THE JOURNAL OF PHYSICAL CHEMISTRY LETTERS
A JOURNAL OF THE AMERICAN CHEMICAL SOCIETY

pubs.acs.org/JPCL

Letter

Metal Halide Perovskite Nanocrystals for Near-Infrared Circularly Polarized Luminescence with High Photoluminescence Quantum Yield via Chiral Ligand Exchange

Jianwu Wei, Qiulian Luo, Sengui Liang, Liya Zhou, Peican Chen, Qi Pang,* and Jin Zhong Zhang

Cite This: *J. Phys. Chem. Lett.* 2023, 14, 5489−5496

Read Online

ACCESS | Metrics & More | Article Recommendations | Supporting Information

ABSTRACT: Using ligand exchange on $FAPbI_3$ perovskite nanocrystals (PNCs) surface with chiral tridentate L-cysteine (L-cys) ligand, we successfully prepared chiral $FAPbI_3$ PNCs that show circularly polarized luminescence (CPL) (dissymmetry factor; $g_{lum} = 2.1 \times 10^{-3}$) in the near-infrared (NIR) region from 700 to 850 nm and a photoluminescence quantum yield (PLQY) of 81%. The chiral characteristics of $FAPbI_3$ PNCs are ascribed to induction by chiral L/D-cys, and the high PLQY is attributed to the passivation of the PNCs defects with L-cys. Also, effective passivation of defects on the surface of $FAPbI_3$ PNCs by L-cys results in excellent stability toward atmospheric water and oxygen. The conductivity of the L-cys treated $FAPbI_3$ NC films is improved, which is attributed to the partial substitution of L-cys for the insulating long oleyl ligand. The CPL of the L-cys ligand treated $FAPbI_3$ PNCs film retains a g_{lum} of -2.7×10^{-4}. This study demonstrates a facile yet effective approach to generating chiral PNCs with CPL for NIR photonics applications.

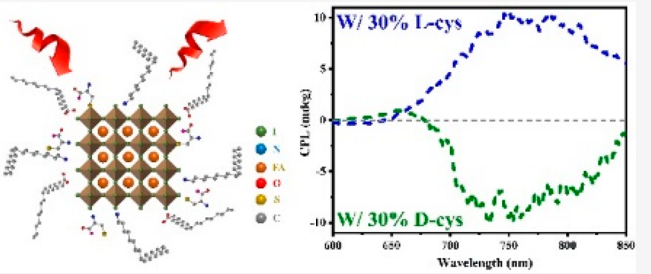

As one of the novel optical properties of chiral materials, circularly polarized luminescence (CPL) in different wavelength regions is of strong interest in photonics applications.[1−3] In particular, the near-infrared (NIR) CPL has potential applications in chiral synthesis, biology, and communication, attributed to its combination of chiral characteristics and high penetration.[4−6] To date, few NIR CPL materials have been reported, mainly based on lanthanide complexes,[5,7] organic helical polymers,[8,9] and small organic molecules (SOM).[10,11] However, these materials suffer from a low photoluminescence quantum yield (PLQY) and complex preparation. The lanthanide complexes tend to have a relatively high dissymmetry factor (g_{lum}) besides low PLQY, which is attributed to the Laporte-forbidden nature.[12,13] Meanwhile, according to energy gap theory, the design of organic molecules for superior NIR CPL (650−900 nm) is highly difficult.[9,14] Both helical polymers and SOM used for NIR CPL have low PLQY as well as requiring tedious preparation.[8−11]

Metal halide perovskites have great potential for superior NIR CPL due to their extreme brightness, high PLQY, and coverage of visible to NIR optical emission.[15,16] Outstanding chiral properties can be obtained through the regulation of nanostructure, the incorporation of chiral ligands, or the change of chemical environment.[17−19] Among them, the incorporation of chiral ligands has become a popular approach to realize chiral perovskite nanocrystals (PNCs) because of its low cost and easy implementation.[1,20,21] Some chiral ligand-induced PNCs have been reported for CPL, which have mainly concentrated in the visible region.[22−24]

In this work, we prepared $FAPbI_3$ PNCs with induced CPL in the NIR region using ligand exchange. In the process of $FAPbI_3$ PNCs synthesis, the conventional oleyl ligands (oleylamine (OAm) or oleic acid (OA)) are partially replaced by chiral tridentate L-cysteine (L-cys) ligands, which not only induce CPL of PNCs due to the chiral characteristics of L-cys but also effectively passivate the surface defects.[25−27] The CPL tests have shown that L-cys treated $FAPbI_3$ PNCs exhibit a CPL signal between 700 and 850 nm and a maximum g_{lum} of 2.1×10^{-3}, while the PLQY of PNCs reaches 81%. Moreover, the time-dependent PL and X-ray diffraction (XRD) indicate that the L-cys treated $FAPbI_3$ PNCs have excellent stability toward water and oxygen. In addition, we additionally prepare thin films of $FAPbI_3$ PNCs using L-cys postprocessing to explore their potential for applications in spintronics devices. The electrochemical impedance spectroscopy (EIS) and CPL measurements of their films show that the conductivity of the L-cys treated $FAPbI_3$ NCs films is improved while the CPL features are retained with a maximum g_{lum} of -2.7×10^{-4}.

Received: May 2, 2023
Accepted: June 6, 2023

https://doi.org/10.1021/acs.jpclett.3c01184
J. Phys. Chem. Lett. 2023, 14, 5489−5496

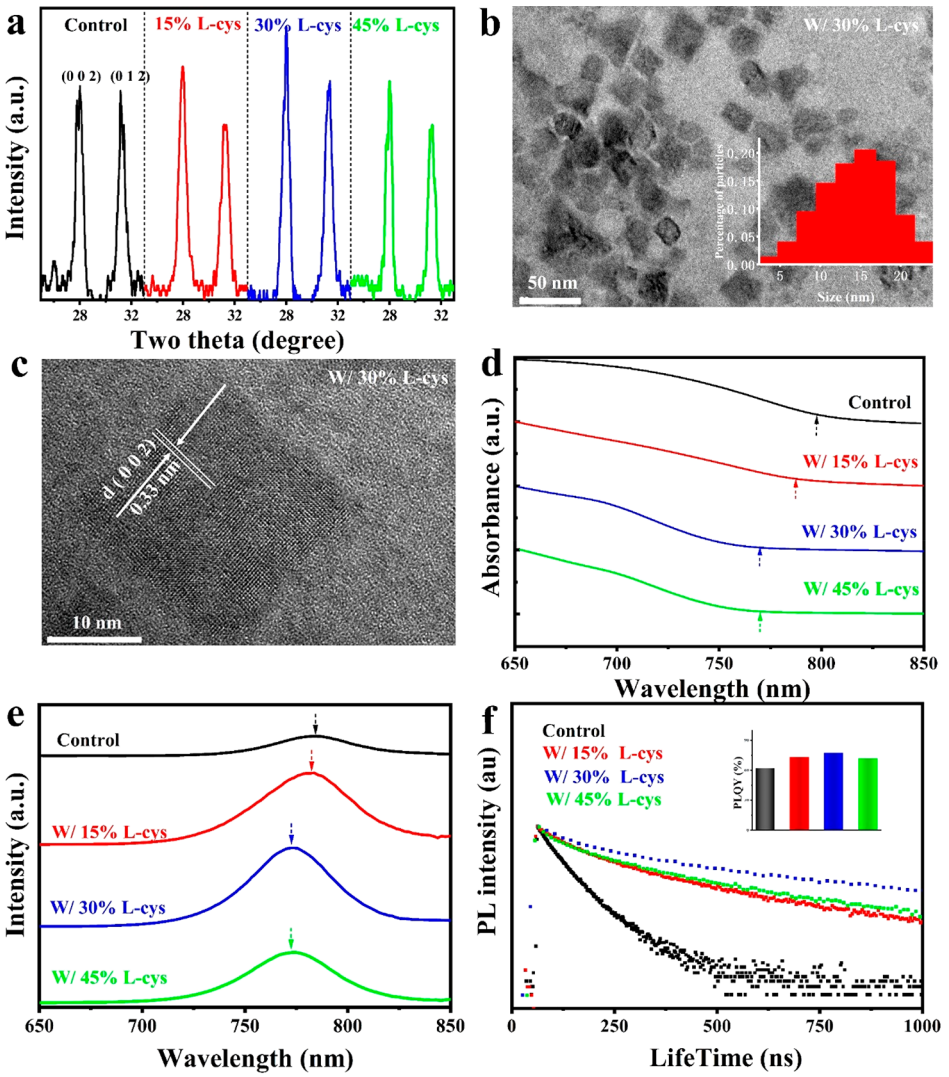

Figure 1. a) XRD patterns, b) TEM, c) HRTEM, d) UV−vis absorption, e) PL spectra (excited by 365 nm), and f) TRPL (excited by 405 nm) of the control and the L-cys treated $FAPbI_3$ PNCs (15 mg/mL in toluene).

The hot injection method was used to synthesize the $FAPbI_3$ nanocrystal.[28,29] Meanwhile, L-cys was directly added in the process of synthesizing nanocrystals. The effect of L-cys on the crystallization process of $FAPbI_3$ PNCs was investigated by XRD. Figure S1 shows the XRD of all concentrations of L-cys treated $FAPbI_3$ PNCs, which are all maintained in the cubic phase. Furthermore, locally amplified XRD is shown in Figure 1a, demonstrating that the relative strength of the (0 0 2) diffraction peak of $FAPbI_3$ PNCs after L-cys treatment is enhanced. This predicts that L-cys does not disrupt the crystal structure of $FAPbI_3$ while directing its crystal selective growth along the (0 0 2) plane to form relatively small-sized nanocrystals, which may be more stable.[30,31]

Transmission electron microscopy (TEM) was used to further investigate the $FAPbI_3$ PNCs. As shown in Figure 1b and Figure S2, the $FAPbI_3$ PNCs treated with 15%, 30%, and 45% L-cys had an average grain size of 35.1 16.5, and 19.5 nm, respectively, while the control PNCs had larger PNCs with an average grain size of 55.4 nm (Figure S3). This can be attributed to the fact that L-cys forms more stable coordination interactions with the nanocrystal surface than the oleyl ligand, thus preventing their further growth and reducing nanocrystal size.[32] Furthermore, the HRTEM of 30% L-cys treated $FAPbI_3$ PNCs in Figure 1c reveals the lattice stripe corresponding to the (0 0 2) plane of the cubic structure, which agrees with the XRD outcome.[29]

We used UV−vis absorption to evaluate the effect of L-cys as a surface ligand on the $FAPbI_3$ PNCs. As seen in Figure. 1d, there is a blue shift in the absorption band edge of the $FAPbI_3$ nanocrystal as the percentage of L-cys added increases from 0% to 45%. The PL intensity of L-cys treated $FAPbI_3$ PNCs is shown in Figure 1e, which also appears to be blue-shifted. This is consistent with the TEM results, where the nanocrystal size reduction leads to the blue-shifted phenomenon.[33,34] It is attributed to the size-dependent bandgap variation from quantum confinement. Moreover, the PL intensity of L-cys treated $FAPbI_3$ PNCs is enhanced compared to the control sample (Figure 1e). This is attributed to the fact that short-chain ligands L-cys can overcome the steric hindrance brought by long-chain ligands (OAm or OA) to approach the surface of nanocrystals, effectively passivating defects and reducing nonradiative recombination.[35]

We further investigated the time-resolved PL (TRPL) of L-cys treated $FAPbI_3$ PNCs, as shown in Figure 1f. The double-exponential function is used to fit the TRPL curve well,[36] and all parameters are listed in Table S1. Compared with control

https://doi.org/10.1021/acs.jpclett.3c01184
J. Phys. Chem. Lett. 2023, 14, 5489−5496

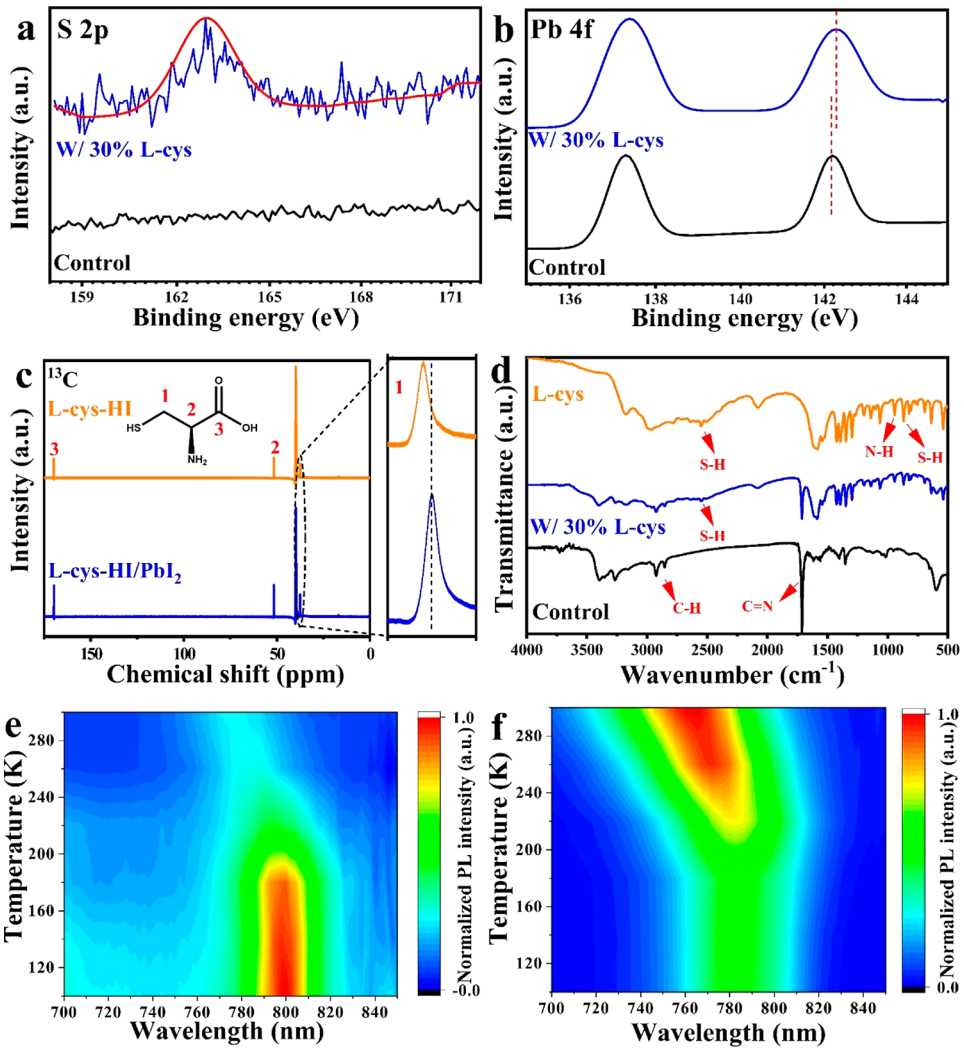

Figure 2. XPS spectra of a) S 2p and b) Pb 4f for the control and the L-cys treated $FAPbI_3$ PNCs, c) liquid-state ^{13}C NMR of the L-cys-HI/PbI_2 mixture in DMSO-d_6, d) FTIR spectra, and e) and f) projection mapping of temperature-dependent photoluminescence of the control and the L-cys treated $FAPbI_3$ PNCs.

PNCs, all concentrations of L-cys treated $FAPbI_3$ PNCs show a longer average carrier lifetime (τ_{avg}). Moreover, the optimal passivation effect is achieved when the content of L-cys reaches 30%. The 30% L-cys treated $FAPbI_3$ PNCs have the longest τ_{avg} of 252.6 ns, wherever the control PNCs have a τ_{avg} of 39.1 ns (Table S1). This indicates that the nonradiative recombination of $FAPbI_3$ PNCs is maximally suppressed when 30% L-cys is used for ligand exchange on it. Meanwhile, PLQY is adopted to further explore the passivation effect of L-cys on the surface defects of $FAPbI_3$ PNCs. The original data are shown in Figure S4, and the comparison of PLQY values of $FAPbI_3$ PNCs treated with different contents of L-cys is shown in Figure 1f. The 30% L-cys treated $FAPbI_3$ PNCs have a champion PLQY (81%), wherever the control PNCs get a PLQY of 60%. This is consistent with the TRPL as well as PL findings that the radiative recombination of 30% L-cys treated $FAPbI_3$ PNCs is improved. The $FAPbI_3$ PNCs treated with excessive L-cys (45%) obtained lower PLQY (72%), which may be attributed to the change of the coordination mode between L-cys and $FAPbI_3$ PNCs surface under high concentrations of L-cys, which eventually led to an unexpected effect.[25]

Figure 2a,b shows the X-ray Photoelectron Spectroscopy (XPS) analysis of the control and L-cys treated $FAPbI_3$ PNCs. The high-resolution XPS spectra of S 2p, Pb 4f, and I 3d are calibrated with C 1s. As shown in Figure 2a, the S 2p characteristic peak belonging to L-cys is detected at 163.28 eV in L-cys treated $FAPbI_3$ PNCs. This indicates that L-cys is successfully attached to the surface of $FAPbI_3$ PNCs.[27,37] Moreover, Figure 2b shows that the $4f_{7/2}$ and $4f_{5/2}$ of L-cys treated $FAPbI_3$ PNCs move toward higher binding energies to 137.38 and 142.28 eV, respectively, compared to the $4f_{7/2}$ at 137.29 eV and $4f_{5/2}$ at 142.19 eV of the Pb 4f spectrum in control PNCs. This is due to the strong chemical bonding effect between L-cys and $FAPbI_3$ PNCs, which leads to changes in the chemical environment on the surface of $FAPbI_3$ PNCs.[37,38] Meanwhile, as shown in Figure S5, the peaks of the $3d_{5/2}$ and $3d_{3/2}$ of the I 3d spectrum in L-cys treated $FAPbI_3$ PNCs shift to 618.16 and 629.62 eV, respectively, wherever the peaks of control PNCs are located at 618.08 and 629.47 eV. This is caused by the changed chemical bond between Pb and I, which is influenced by the chemical bond effect between Pb and S.[27] We additionally employed liquid-state ^{13}C NMR to probe the chemical coordination effects between Pb and S by characterizing the L-cys/PbI_2 mixture in Figure 2c. The chemical shift of S-linked C in pure L-cys induces a downfield chemical shift in the L-cys/PbI_2 mixture.

https://doi.org/10.1021/acs.jpclett.3c01184
J. Phys. Chem. Lett. 2023, 14, 5489−5496

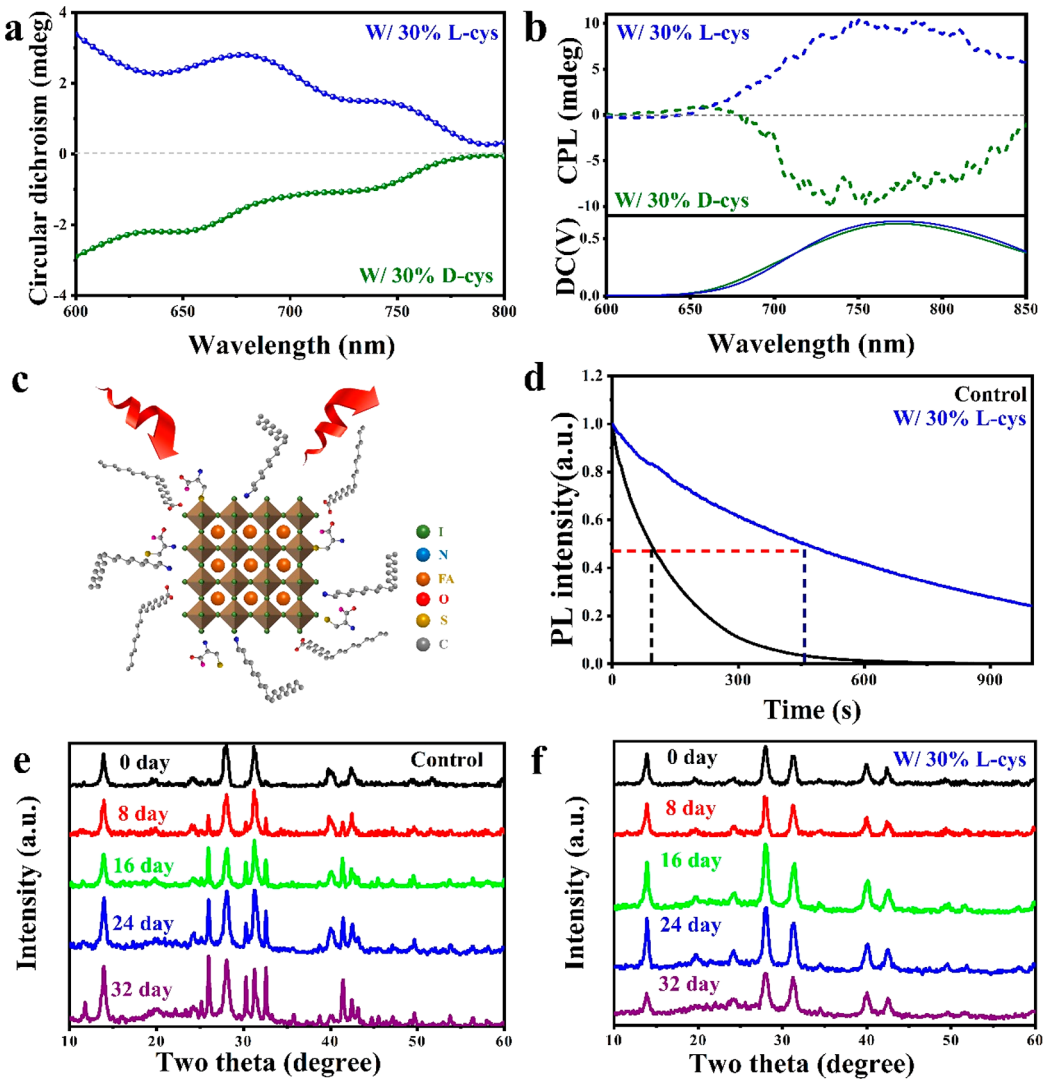

Figure 3. a) CD spectra of L/D-cys treated $FAPbI_3$ PNCs. b) CPL and DC of L/D-cys treated $FAPbI_3$ PNCs (15 mg/mL in toluene) excited by 365 nm. c) Schematic illustrations of L-cys treated $FAPbI_3$ PNCs. d). Time-dependent PL in water. e) and f) Time-dependent XRD for the control $FAPbI_3$ PNCs and the $FAPbI_3$ PNCs with 30% L-cys in the air with an average humidity of 75%.

This is due to the implication of changes in the electron cloud density around the nucleus of the sulfur atom caused by chemical coordination between Pb−S. Figure 2d shows the changes in the Fourier transform infrared (FTIR) spectroscopy of $FAPbI_3$ PNCs after L-cys treatment. Under the condition of keeping the same amount of control and L-cys treated $FAPbI_3$ PNCs used in the preparation of test samples, we observed a decrease in the strength of C−H stretching peaks (2923 and 2856 cm^{-1}) which partially belong to the oleyl ligand.[39] Meanwhile, the absorption peaks at 1059 and 939 cm^{-1} correspond to the N−H rocking vibrational and the S−H bending vibrational, which belong to L-cys and are observed in the infrared spectral fingerprint region of L-cys treated $FAPbI_3$ PNCs.[25] This indicates that the proportion of long-chain ligands on the $FAPbI_3$ PNCs surface is reduced, and L-cys successfully lands on it. Temperature-dependent PL was used to study the effect of L-cys treatment on the thermal stability of $FAPbI_3$ PNCs. The different color plots in Figure 2e,f show the positions and intensities of PL peaks at different temperatures. As shown in Figure 2e,f, starting at temperatures of about 175 K, the PL peak position begins to mutate in both control and L-cys treated $FAPbI_3$ PNCs. This is attributed to the fact that $FAPbI_3$ has a phase transition from the rhombic to the Theodoric phase near 165 K.[40] When the temperature is higher than 175 K, the peak position of $FAPbI_3$ PNCs will significantly shift blue with increasing temperature regardless of whether L-cys is used to treat it. This is due to the widening of the band gap caused by lattice expansion in increasing temperatures.[40−42] In Figure 2e, the PL intensity of control $FAPbI_3$ PNCs decreases with increasing temperature, owing to phonon-assisted relaxation.[42] As shown in Figure 2f, the PL intensity of L-cys treated $FAPbI_3$ PNCs increases with increasing temperature, which is the opposite of control $FAPbI_3$ PNCs. This may be due to the strengthening of the chemical relationship between L-cys and $FAPbI_3$ PNCs as the temperature increases. The sulfur atom in L-cys may serve to fill the iodine vacancy and passivate iodine defects on the surface of $FAPbI_3$ PNCs to improve the photoactivity of $FAPbI_3$ PNCs,[37,43] and this process is thermally activated.[44,45] This phenomenon reveals the possibility of L-cys treated $FAPbI_3$ PNCs for stable operation of LED devices. It seems to maintain high PLQY at the joule heat generated by device operation due to its thermally activated PL.

https://doi.org/10.1021/acs.jpclett.3c01184
J. Phys. Chem. Lett. 2023, 14, 5489−5496

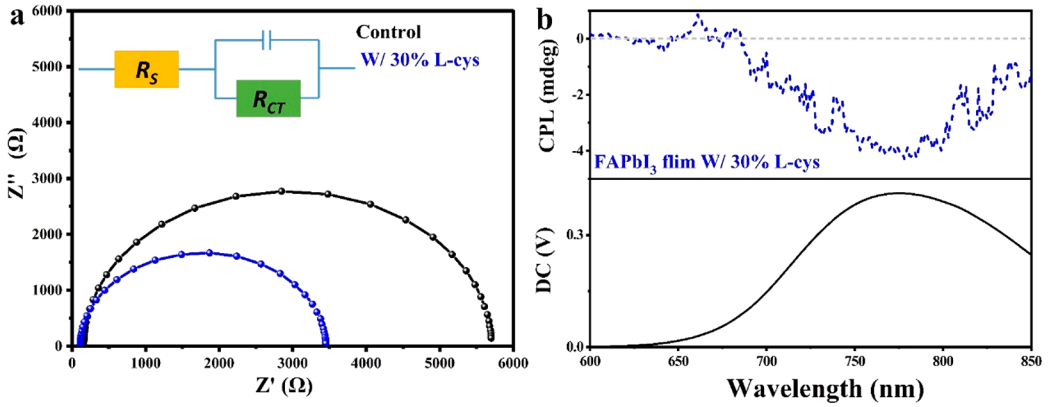

Figure 4. a) EIS of the $FAPbI_3$ PNCs film with and without 30% L-cys. b) CPL and DC of the $FAPbI_3$ PNCs film with 30% L-cys.

As shown in Figure 3a, the circular dichroism (CD) of L/D-cys treated $FAPbI_3$ PNCs is measured to explore the effect of 30% L/D-cys on the optical chirality of $FAPbI_3$ PNCs. The CD spectrum starts to show signals around 760 nm, which is completely different from that of L/D-cys (Figure S6). The intensity of the CD spectrum increases dramatically as the wavelength lowers, most likely due to its positive association with UV−vis absorption.[22,46,47] That means that the CD signal is coming from $FAPbI_3$ PNCs. This proves that CD-active chiral perovskites were successfully induced by L/D-cys's chiral properties.[22] Figure 3b and Figure S7 show further examination of the CPL of $FAPbI_3$ PNCs treated with different amounts of L-cys, demonstrating a DC (nonpolarized fluorescence) spectrum between 700 and 850 nm, which is similar to the PL spectrum. And, the CPL of these $FAPbI_3$ PNCs also displays a signal in the same range, suggesting that L-cys successfully induces the CPL signal of $FAPbI_3$ PNCs. The maximum g_{lum} of the CPL signal was calculated to be 1.3×10^{-3}, 2.1×10^{-3}, and 0.9×10^{-3} for 15%, 30%, and 45% L-cys treated $FAPbI_3$ PNCs respectively, which was measured experimentally using a JASCO CPL-300 spectrometer. As the L-cys content increased, the g_{lum} of $FAPbI_3$ PNCs increased initially and then decreased. This is likely due to the coordination mode between L-cys and $FAPbI_3$ PNCs transitioning from tridentate to bidentate coordination when the L-cys content surpasses 30%, thus affecting the chiral characteristics of $FAPbI_3$ PNCs.[25] Meanwhile, the influence of the synthesis temperature on the CPL of nanocrystals had been investigated. Figure S8 shows the CPL signals of nanocrystals at synthesizing temperatures of 323 and 383 K, corresponding to $g_{lum} = 1.6 \times 10^{-3}$ and 1.9×10^{-3}, respectively. It proves that the synthesis temperature has little effect on the CPL signal, with the g_{lum} value remaining around 10^{-3}. The CPL signal clearly shows little sensitivity to the synthesis temperature, with the g_{lum} value maintaining close. The chiral characteristics of $FAPbI_3$ PNCs may have originated from this process: smaller PNCs produced by L/D-cys modification have a higher surface-to-volume ratio, which, in turn, allows more L-cys to attach to the surface of PNCs. The distance between L/D-cys and the electronic states in the core PNCs is short, which causes L/D-cys treated $FAPbI_3$ PNCs to produce significant lattice distortion[24,48] and electronic coupling[49,50] to produce optical chiral effects.[22] Consequently, the chiral $FAPbI_3$ PNCs can achieve CPL upon excitation, and this process is shown in Figure 3c.

Meanwhile, we explored the effect of L-cys on the stability of the $FAPbI_3$ PNCs. First, as shown in Figure 3d, the PL decay rate of $FAPbI_3$ PNCs dispersed in water is used to measure it. The T_{50} (the time for 50% of peak PL) of L-cys treated $FAPbI_3$ PNCs is extended to 455s, while the T_{50} of control $FAPbI_3$ PNCs is only 90 s. Further, we continuously monitored the XRD of $FAPbI_3$ PNCs exposed to the atmosphere to assess the effect of L-cys on the crystal phase stability of the $FAPbI_3$ PNCs. Figure 3e shows that the hexagonal yellow (δ) phase was quickly observed in the time-dependent XRD of control $FAPbI_3$ PNCs and occupied a dominant position over time.[51,52] And Figure 3f shows that L-cys treated $FAPbI_3$ PNCs remain optically active cubic (α) phases after continuous exposure to the atmosphere for about 30 days. Meanwhile, the optical stability of L-cys treated $FAPbI_3$ PNCs had been investigated. Figure S9 indicates that, after 30 days of storage, the PL intensity had retained 70% of the original peak, in comparison to that of the control $FAPbI_3$ PNCs, which had retained 0.84% of the original peak. The significant improvement in the stability of $FAPbI_3$ PNCs may be attributed to the strong Pb−S chemical coordination effect between L-cys and $FAPbI_3$ PNCs, which stabilizes surface defects of $FAPbI_3$ PNCs and reduces interaction with environmental species such as oxygen and water.[27]

Ultimately, the $FAPbI_3$ PNCs need to be purified to prepare thin films that can be assembled into devices to achieve application value. Overall, the relevant properties of $FAPbI_3$ PNCs in thin film form profoundly affect its prospects for applications in various optoelectronic devices. During the purification process, the $FAPbI_3$ PNCs inevitably lose a large number of surface ligands, resulting in fluorescence quenching. We overcame this by readding L-cys in the purification process. We used EIS to evaluate the charge transport capacity of the $FAPbI_3$ PNCs films. The measurement method reported previously was adopted,[53,54] as shown in Figure S10. Meanwhile, to eliminate the influence of film thickness on the results,[55] a unified spinning coating process was adopted to prepare the film. SEM of the thin film cross-section shows that control and L-cys treated $FAPbI_3$ PNCs film are close in thickness (Figure S11). As shown in Figure 4a, we show the charge-transfer (R_{CT}) ability of the $FAPbI_3$ PNCs film. The L-cys treated $FAPbI_3$ PNCs film has a smaller R_{CT}, which means its charge-transfer ability is improved.[54] This is due to the partial substitution of L-cys for the insulating long oleyl ligand. Moreover, as shown in Figure 4b, we measured the CPL of the L-cys treated $FAPbI_3$ PNCs film, which still maintains CPL at

https://doi.org/10.1021/acs.jpclett.3c01184
J. Phys. Chem. Lett. 2023, 14, 5489−5496

700−800 nm with a maximum g_{lum} of -2.7×10^{-4}. The CPL signal of $FAPbI_3$ PNCs film is the opposite of that of $FAPbI_3$ PNCs colloidal solutions, which could be attributed to the alteration of the chemical environment caused by secondary exchange of ligands on the nanocrystal surfaces, along with rearrangement of nanocrystals due to solvent volatilization during annealing.[56]

In summary, $FAPbI_3$ PNCs with NIR CPL were synthesized by modification with chiral tridentate L-cys ligand during the hot injection method. The CD and CPL tests showed that chirality of $FAPbI_3$ PNCs was successfully induced, and the L-cys treated $FAPbI_3$ PNCs exhibit a CPL signal ranging between 700 and 850 nm and a maximum g_{lum} of 2.1×10^{-3}, while the PLQY of PNCs reaches 81%. TRPL and PLQY measurements showed that defects in $FAPbI_3$ PNCs were reduced after the L-cys treatment. Time-dependent XRD study shows that the L-cys treated $FAPbI_3$ PNCs are stable for over 30 days. In addition, the EIS and CPL of the films show improved conductivity and retained CPL of L-cys treated $FAPbI_3$ PNCs films. This study demonstrates that chiral amino acids can serve as unique short-chain ligands for the synthesis of stable PNCs with CPL.

■ ASSOCIATED CONTENT

Supporting Information

The Supporting Information is available free of charge at https://pubs.acs.org/doi/10.1021/acs.jpclett.3c01184.

Experimental methods, XRD of different concentrations of L-cys treated $FAPbI_3$ PNCs, TEM images of the $FAPbI_3$ PNCs with 15% and 45% L-cys, TEM images of the control $FAPbI_3$ PNCs, TRPL parameters of perovskite from Figure 1f, PLQY of different concentrations of L-cys treated $FAPbI_3$ PNCs, XPS spectra of I 3d for the control $FAPbI_3$ PNCs and the L-cys treated $FAPbI_3$ PNCs, CD spectrum of L-cys and D-cys, CPL and DC value of 15% and 45% L-cys treated $FAPbI_3$ PNCs, CPL and DC value of 30% L-cys treated $FAPbI_3$ PNCs at different hot injection temperatures, time-dependent PL of $FAPbI_3$ PNCs, EIS of the $FAPbI_3$ PNCs film with and without 30% L-cys, electrochemical impedance spectroscopy measurement, SEM of the thin film cross-section (PDF)

■ AUTHOR INFORMATION

Corresponding Author

Qi Pang − *School of Chemistry and Chemical Engineering, and Guangxi Key Laboratory of Petrochemical Resource Processing and Process Intensification Technology, Guangxi University, Nanning 530004 Guangxi, China;* orcid.org/0000-0002-5190-1250; Email: pqigx@163.com

Authors

Jianwu Wei − *School of Chemistry and Chemical Engineering, and Guangxi Key Laboratory of Petrochemical Resource Processing and Process Intensification Technology, Guangxi University, Nanning 530004 Guangxi, China*

Qiulian Luo − *School of Chemistry and Chemical Engineering, and Guangxi Key Laboratory of Petrochemical Resource Processing and Process Intensification Technology, Guangxi University, Nanning 530004 Guangxi, China*

Sengui Liang − *School of Chemistry and Chemical Engineering, and Guangxi Key Laboratory of Petrochemical Resource Processing and Process Intensification Technology, Guangxi University, Nanning 530004 Guangxi, China*

Liya Zhou − *School of Chemistry and Chemical Engineering, and Guangxi Key Laboratory of Petrochemical Resource Processing and Process Intensification Technology, Guangxi University, Nanning 530004 Guangxi, China;* orcid.org/0000-0002-0581-034X

Peican Chen − *School of Chemistry and Chemical Engineering, and Guangxi Key Laboratory of Petrochemical Resource Processing and Process Intensification Technology, Guangxi University, Nanning 530004 Guangxi, China*

Jin Zhong Zhang − *Department of Chemistry and Biochemistry, University of California, Santa Cruz, California 95064, United States;* orcid.org/0000-0003-3437-912X

Complete contact information is available at: https://pubs.acs.org/10.1021/acs.jpclett.3c01184

Notes

The authors declare no competing financial interest.

■ ACKNOWLEDGMENTS

This work was supported by the National Natural Science Foundation of China (Grant No. 21965003) and the Opening Project of Guangxi Key Laboratory of Petrochemical Resource Processing and Process Intensification Technology (Grant No. 2022K008). J.Z.Z. acknowledges the US NSF (CHE-2203633) for financial support.

■ REFERENCES

(1) Gong, Z. L.; Zhu, X.; Zhou, Z.; Zhang, S. W.; Yang, D.; Zhao, B.; Zhang, Y. P.; Deng, J.; Cheng, Y.; Zheng, Y. X.; et al. Frontiers in circularly polarized luminescence: molecular design, self-assembly, nanomaterials, and applications. *Sci. China Chem.* **2021**, *64* (12), 2060−2104.

(2) Ma, J.; Wang, H.; Li, D. Recent progress of chiral perovskites: materials, synthesis, and properties. *Adv. Mater.* **2021**, *33* (26), No. e2008785.

(3) Jiang, S.; Kotov, N. A. Circular polarized light emission in chiral inorganic nanomaterials. *Adv. Mater.* **2022**, No. e2108431.

(4) Yang, G.; Zhu, L.; Hu, J.; Xia, H.; Qiu, D.; Zhang, Q.; Zhang, D.; Zou, G. Near-infrared circularly polarized light triggered enantioselective photopolymerization by using upconversion nanophosphors. *Chem.—Eur. J.* **2017**, *23* (33), 8032−8038.

(5) Zinna, F.; Arrico, L.; Di Bari, L. Near-infrared circularly polarized luminescence from chiral Yb(iii)-diketonates. *Chem. Commun.* **2019**, *55* (46), 6607−6609.

(6) Liu, L.; Yang, Y.; Zhu, L.; Zhang, J.; Chen, K.; Wei, Z. Chiral non-fullerene acceptor enriched bulk heterojunctions enable high-performance near-infrared circularly polarized light detection. *Small* **2022**, *18* (31), No. e2202941.

(7) Mukthar, N. F. M.; Schley, N. D.; Ung, G. Strong circularly polarized luminescence at 1550 nm from enantiopure molecular erbium complexes. *J. Am. Chem. Soc.* **2022**, *144* (14), 6148−6153.

(8) Míguez-Lago, S.; Mariz, I. F. A.; Medel, M. A.; Cuerva, J. M.; Maçôas, E.; Cruz, C. M.; Campaña, A. G. Highly contorted superhelicene hits near-infrared circularly polarized luminescence. *Chem. Sci.* **2022**, *13* (35), 10267−10272.

(9) Xu, Y.; Ni, Z.; Xiao, Y.; Chen, Z.; Wang, S.; Gai, L.; Zheng, Y.-X.; Shen, Z.; Lu, H.; Guo, Z. Helical β-isoindigo-based chromophores with b-o-b bridge: facile synthesis and tunable near-infrared circularly polarized luminescence. *Angew. Chem., Int. Ed.* **2023**, *62* (8), No. e202218023.

(10) Feng, J.; Fu, L.; Geng, H.; Jiang, W.; Wang, Z. Designing a near-infrared circularly polarized luminescent dye by dissymmetric spiro-fusion. *Chem. Commun.* **2020**, *56* (6), 912−915.
(11) Jiménez, J.; Díaz-Norambuena, C.; Serrano, S.; Ma, S. C.; Moreno, F.; Maroto, B. L.; Bañuelos, J.; Muller, G.; de la Moya, S. BINOLated aminostyryl BODIPYs: a workable organic molecular platform for NIR circularly polarized luminescence. *Chem. Commun.* **2021**, *57* (47), 5750−5753.
(12) Kubo, H.; Hirose, T.; Nakashima, T.; Kawai, T.; Hasegawa, J.-y.; Matsuda, K. Tuning transition electric and magnetic dipole moments: [7]helicenes showing intense circularly polarized luminescence. *J. Phys. Chem. Lett.* **2021**, *12* (1), 686−695.
(13) Zhang, J.; Dai, L.; Webster, A. M.; Chan, W. T. K.; Mackenzie, L. E.; Pal, R.; Cobb, S. L.; Law, G.-L. Unusual magnetic field responsive circularly polarized luminescence probes with highly emissive chiral europium(iii) complexes. *Angew. Chem., Int. Ed.* **2021**, *60* (2), 1004−1010.
(14) Erker, C.; Basché, T. The energy gap law at work: emission yield and rate fluctuations of single nir emitters. *J. Am. Chem. Soc.* **2022**, *144* (31), 14053−14056.
(15) Bai, Y.; Hao, M.; Ding, S.; Chen, P.; Wang, L. Surface chemistry engineering of perovskite quantum dots: strategies, applications, and perspectives. *Adv. Mater.* **2022**, *34* (4), 2105958.
(16) Dong, Y.; Zhang, Y.; Li, X.; Feng, Y.; Zhang, H.; Xu, J. Chiral perovskites: promising materials toward next-generation optoelectronics. *Small* **2019**, *15* (39), No. e1902237.
(17) Long, G.; Sabatini, R.; Saidaminov, M. I.; Lakhwani, G.; Rasmita, A.; Liu, X.; Sargent, E. H.; Gao, W. Chiral-perovskite optoelectronics. *Nat. Rev. Mater.* **2020**, *5* (6), 423−439.
(18) Long, G.; Jiang, C.; Sabatini, R.; Yang, Z.; Wei, M.; Quan, L. N.; Liang, Q.; Rasmita, A.; Askerka, M.; Walters, G.; et al. Spin control in reduced-dimensional chiral perovskites. *Nat. Photonics* **2018**, *12* (9), 528−533.
(19) Long, G.; Adamo, G.; Tian, J.; Klein, M.; Krishnamoorthy, H. N. S.; Feltri, E.; Wang, H.; Soci, C. Perovskite metasurfaces with large superstructural chirality. *Nat. Commun.* **2022**, *13* (1), 1551.
(20) Han, T.-H.; Jang, K. Y.; Dong, Y.; Friend, R. H.; Sargent, E. H.; Lee, T.-W. A roadmap for the commercialization of perovskite light emitters. *Nat. Rev. Mater.* **2022**, *7* (10), 833−833.
(21) Liu, L.; Pan, K.; Xu, K.; Zhang, J. Z. Impact of molecular ligands in the synthesis and transformation between metal halide perovskite quantum dots and magic sized clusters. *ACS Phys. Chem. Au* **2022**, *2* (3), 156−170.
(22) Kim, Y. H.; Zhai, Y.; Gaulding, E. A.; Habisreutinger, S. N.; Moot, T.; Rosales, B. A.; Lu, H.; Hazarika, A.; Brunecky, R.; Wheeler, L. M.; et al. Strategies to achieve high circularly polarized luminescence from colloidal organic-inorganic hybrid perovskite nanocrystals. *ACS Nano* **2020**, *14* (7), 8816−8825.
(23) Jiang, S.; Song, Y.; Kang, H.; Li, B.; Yang, K.; Xing, G.; Yu, Y.; Li, S.; Zhao, P.; Zhang, T. Ligand exchange strategy to achieve chiral perovskite nanocrystals with a high photoluminescence quantum yield and regulation of the chiroptical property. *ACS Appl. Mater. Interfaces* **2022**, *14* (2), 3385−3394.
(24) Chen, W.; Zhang, S.; Zhou, M.; Zhao, T.; Qin, X.; Liu, X.; Liu, M.; Duan, P. Two-photon absorption-based upconverted circularly polarized luminescence generated in chiral perovskite nanocrystals. *J. Phys. Chem. Lett.* **2019**, *10* (12), 3290−3295.
(25) Kuznetsova, V. A.; Mates-Torres, E.; Prochukhan, N.; Marcastel, M.; Purcell-Milton, F.; O'Brien, J.; Visheratina, A. K.; Martinez-Carmona, M.; Gromova, Y.; Garcia-Melchor, M.; et al. Effect of chiral ligand concentration and binding mode on chiroptical activity of CdSe/Cds quantum dots. *ACS Nano* **2019**, *13* (11), 13560−13572.
(26) Lee, H. E.; Ahn, H. Y.; Mun, J.; Lee, Y. Y.; Kim, M.; Cho, N. H.; Chang, K.; Kim, W. S.; Rho, J.; Nam, K. T. Amino-acid- and peptide-directed synthesis of chiral plasmonic gold nanoparticles. *Nature* **2018**, *556* (7701), 360−365.
(27) Huynh, K. A.; Bae, S.-R.; Nguyen, T. V.; Do, H. H.; Heo, D. Y.; Park, J.; Lee, T.-W.; Le, Q. V.; Ahn, S. H.; Kim, S. Y. Ligand-assisted sulfide surface treatment of $CsPbI_3$ perovskite quantum dots to increase photoluminescence and recovery. *ACS Photonics* **2021**, *8* (7), 1979−1987.
(28) Papagiorgis, P.; Manoli, A.; Protesescu, L.; Achilleos, C.; Violaris, M.; Nicolaides, K.; Trypiniotis, T.; Bodnarchuk, M. I.; Kovalenko, M. V.; Othonos, A.; et al. Efficient optical amplification in the nanosecond regime from formamidinium lead iodide nanocrystals. *ACS Photonics* **2018**, *5* (3), 907−917.
(29) Que, M.; Dai, Z.; Yang, H.; Zhu, H.; Zong, Y.; Que, W.; Padture, N. P.; Zhou, Y.; Chen, O. Quantum-dot-induced cesium-rich surface imparts enhanced stability to formamidinium lead iodide perovskite solar cells. *ACS Energy Lett.* **2019**, *4* (8), 1970−1975.
(30) Li, B.; Shen, T.; Yun, S. Recent progress of crystal orientation engineering in halide perovskite photovoltaics. *Mater. Horizons* **2023**, *10* (1), 13−40.
(31) Ding, C.; Liu, F.; Zhang, Y.; Hirotani, D.; Rin, X.; Hayase, S.; Minemoto, T.; Masuda, T.; Wang, R.; Shen, Q. Photoexcited hot and cold electron and hole dynamics at $FAPbI_3$ perovskite quantum dots/metal oxide heterojunctions used for stable perovskite quantum dot solar cells. *Nano Energy* **2020**, *67*, 104267.
(32) McGrath, F.; Ghorpade, U. V.; Ryan, K. M. Synthesis and dimensional control of $CsPbBr_3$ perovskite nanocrystals using phosphorous based ligands. *J. Chem. Phys.* **2020**, *152* (17), 174702.
(33) Das, T. K.; Ilaiyaraja, P.; Sudakar, C. Whispering gallery mode enabled efficiency enhancement: defect and size controlled cdse quantum dot sensitized whisperonic solar cells. *Sci. Rep* **2018**, *8* (1), 9709.
(34) Kim, Y. H.; Wolf, C.; Kim, Y. T.; Cho, H.; Kwon, W.; Do, S.; Sadhanala, A.; Park, C. G.; Rhee, S. W.; Im, S. H.; et al. Highly efficient light-emitting diodes of colloidal metal-halide perovskite nanocrystals beyond quantum size. *ACS Nano* **2017**, *11* (7), 6586−6593.
(35) Chen, S.; Wei, J.; Pang, Q. Enhancing photoluminescence and stability of $CsPbI_3$ perovskite quantum dots via cysteine post-processing. *Crystals* **2023**, *13* (1), 45.
(36) Hu, Y.; Yan, X.; Zhou, L.; Chen, P.; Pang, Q.; Chen, Y. Improved energy transfer in mn-doped $Cs_3Cu_2I_5$ microcrystals induced by localized lattice distortion. *J. Phys. Chem. Lett.* **2022**, *13* (46), 10786−10792.
(37) Chen, D.; Ko, P. K.; Li, C. H. A.; Zou, B.; Geng, P.; Guo, L.; Halpert, J. E. Amino acid-passivated pure red $CsPbI_3$ quantum dot leds. *ACS Energy Lett.* **2023**, *8* (1), 410−416.
(38) Yang, S.; Chen, S.; Mosconi, E.; Fang, Y.; Xiao, X.; Wang, C.; Zhou, Y.; Yu, Z.; Zhao, J.; Gao, Y.; et al. Stabilizing halide perovskite surfaces for solar cell operation with wide-bandgap lead oxysalts. *Science* **2019**, *365* (6452), 473−478.
(39) Xue, J.; Lee, J.-W.; Dai, Z.; Wang, R.; Nuryyeva, S.; Liao, M. E.; Chang, S.-Y.; Meng, L.; Meng, D.; Sun, P.; et al. Surface ligand management for stable $FAPbI_3$ perovskite quantum dot solar cells. *Joule* **2018**, *2* (9), 1866−1878.
(40) Wright, A. D.; Verdi, C.; Milot, R. L.; Eperon, G. E.; Perez-Osorio, M. A.; Snaith, H. J.; Giustino, F.; Johnston, M. B.; Herz, L. M. Electron-phonon coupling in hybrid lead halide perovskites. *Nat. Commun.* **2016**, *7*, 11755.
(41) Jiang, B.; Chen, S. L.; Cui, X. L.; Hu, Z. T.; Li, Y.; Zhang, X. Z.; Wu, K. J.; Wang, W. Z.; Jiang, Z. M.; Hong, F.; et al. Temperature-dependent photoluminescence in hybrid iodine-based perovskites film. *Acta Phys. Sin-Ch ed* **2019**, *68* (24), 246801.
(42) Liu, N.; Sun, R.; Wang, L.; Ji, Y.; Li, N.; Cao, B.; Zhang, Y. Unexpected red emission from Cs_4PbI_6 nanocrystals. *J. Mater. Chem. A* **2020**, *8* (12), 5952−5958.
(43) Li, J.; Chen, Z.; Saha, S.; Utterback, J. K.; Aubrey, M. L.; Yuan, R.; Weaver, H. L.; Ginsberg, N. S.; Chapman, K. W.; Filip, M. R.; et al. Zwitterions in 3D perovskites: organosulfide-halide perovskites. *J. Am. Chem. Soc.* **2022**, *144* (49), 22403−22408.
(44) Pinchetti, V.; Anand, A.; Akkerman, Q. A.; Sciacca, D.; Lorenzon, M.; Meinardi, F.; Fanciulli, M.; Manna, L.; Brovelli, S. Trap-mediated two-step sensitization of manganese dopants in perovskite nanocrystals. *ACS Energy Lett.* **2019**, *4* (1), 85−93.

https://doi.org/10.1021/acs.jpclett.3c01184
J. Phys. Chem. Lett. 2023, 14, 5489−5496

(45) Luo, B.; Guo, Y.; Li, X.; Xiao, Y.; Huang, X.; Zhang, J. Z. Efficient trap-mediated Mn^{2+} dopant emission in two dimensional single-layered perovskite $(CH_3CH_2NH_3)_2PbBr_4$. *J. Phys. Chem. C* **2019**, *123* (23), 14239−14245.
(46) Chen, W.; Zhang, S.; Zhou, M.; Zhao, T.; Qin, X.; Liu, X.; Liu, M.; Duan, P. Two-photon absorption-based upconverted circularly polarized luminescence generated in chiral perovskite nanocrystals. *J. Phys. Chem. Lett.* **2019**, *10* (12), 3290−3295.
(47) Liu, P.; Battie, Y.; Kimura, T.; Okazaki, Y.; Pranee, P.; Wang, H.; Pouget, E.; Nlate, S.; Sagawa, T.; Oda, R. Chiral perovskite nanocrystal growth inside helical hollow silica nanoribbons. *Nano Lett.* **2023**, *23* (8), 3174−3180.
(48) Kim, Y. H.; Song, R. Y.; Hao, J.; Zhai, Y. X.; Yan, L.; Moot, T.; Palmstrom, A. F.; Brunecky, R.; You, W.; Berry, J. J.; et al. The structural origin of chiroptical properties in perovskite nanocrystals with chiral organic ligands. *Adv. Funct. Mater.* **2022**, *32* (25), 2200454.
(49) Ben Moshe, A.; Szwarcman, D.; Markovich, G. Size dependence of chiroptical activity in colloidal quantum dots. *ACS Nano* **2011**, *5* (11), 9034−9043.
(50) Yao, H.; Miki, K.; Nishida, N.; Sasaki, A.; Kimura, K. Karge optical activity of gold nanocluster enantiomers induced by a pair of optically active penicillamines. *J. Am. Chem. Soc.* **2005**, *127* (44), 15536−15543.
(51) Lu, H.; Liu, Y.; Ahlawat, P.; Mishra, A.; Tress, W. R.; Eickemeyer, F. T.; Yang, Y.; Fu, F.; Wang, Z.; Avalos, C. E.; et al. Vapor-assisted deposition of highly efficient, stable black-phase FAPbI(3) perovskite solar cells. *Science* **2020**, *370* (6512), 74.
(52) Xie, L.-Q.; Chen, L.; Nan, Z.-A.; Lin, H.-X.; Wang, T.; Zhan, D.-P.; Yan, J.-W.; Mao, B.-W.; Tian, Z.-Q. Understanding the cubic phase stabilization and crystallization kinetics in mixed cations and halides perovskite single crystals. *J. Am. Chem. Soc.* **2017**, *139* (9), 3320−3323.
(53) Samu, G. F.; Scheidt, R. A.; Kamat, P. V.; Janáky, C. Electrochemistry and spectroelectrochemistry of lead halide perovskite films: materials science aspects and boundary conditions. *Chem. Mater.* **2018**, *30* (3), 561−569.
(54) Vickers, E. T.; Graham, T. A.; Chowdhury, A. H.; Bahrami, B.; Dreskin, B. W.; Lindley, S.; Naghadeh, S. B.; Qiao, Q.; Zhang, J. Z. Improving charge carrier delocalization in perovskite quantum dots by surface passivation with conductive aromatic ligands. *ACS Energy Lett.* **2018**, *3* (12), 2931−2939.
(55) Saif, A. e. A.; Poopalan, P. Effect of the film thickness on the impedance behavior of sol-gel $Ba_{0.6}Sr_{0.4}TiO_3$ thin films. *Physica B* **2011**, *406* (6), 1283−1288.
(56) Yuan, Y.-X.; Hu, M.; Zhang, K.-R.; Zhou, T.-T.; Wang, S.; Liu, M.; Zheng, Y.-S. The largest CPL enhancement by further assembly of self-assembled superhelices based on the helical TPE macrocycle. *Mater. Horiz.* **2020**, *7* (12), 3209−3216.

https://doi.org/10.1021/acs.jpclett.3c01184
J. Phys. Chem. Lett. 2023, 14, 5489−5496